Published in final edited form as:
J Neuropathol Exp Neurol. 2009 September ; 68(9): 1037–1048. doi:10.1097/NEN.0b013e3181b5417e.

Demyelinated Axons And Motor Function Are Protected by Genetic Deletion of Perforin in a Mouse Model of Multiple Sclerosis

Chandra Deb, PhD[1], **Reghann G. LaFrance-Corey, MSc**[1], **Laurie Zoecklein, MSc**[1], **Louisa Papke, BSc**[1], **Moses Rodriguez, MD**[1,3], and **Charles L. Howe, PhD**[1,2,3,4,5,*]

[1]Department of Neurology, Mayo Clinic College of Medicine, Rochester, MN, USA 55905

[2]Department of Neuroscience, Mayo Clinic College of Medicine, Rochester, MN, USA 55905

[3]Department of Immunology, Mayo Clinic College of Medicine, Rochester, MN, USA 55905

[4]Department of Translational Immunovirology and Biodefense Program, Mayo Clinic College of Medicine, Rochester, MN, USA 55905

[5]Department of Molecular Neuroscience Program, Mayo Clinic College of Medicine, Rochester, MN, USA 55905

Abstract

Axon injury is a major determinant of the loss of neurologic function in patients with multiple sclerosis (MS). It is unclear, however, whether damage to axons is an obligatory consequence of demyelination or whether it is an independent process that occurs in the permissive environment of demyelinated lesions. Previous investigations into the role of $CD8^+$ T cells and perforin in the Theiler's murine encephalomyelitis virus (TMEV) model of MS have used mouse strains resistant to TMEV infection. To test the role of $CD8^+$ T cells in axon injury, we established a perforin-deficient mouse model on the H-2^q MHC background thereby removing confounding factors related to viral biology in this TMEV-susceptible strain. This permitted direct comparison of clinical and pathological parameters between perforin-competent and perforin-deficient mice. The extent of demyelination was indistinguishable between perforin-competent and perforin-deficient H-2^q mice but chronically infected perforin-deficient mice exhibited preservation of motor function and spinal axons despite the presence of spinal cord demyelination. Thus, demyelination is necessary but insufficient for axon injury in this model; the absence of perforin protects axons without impacting demyelination. These results suggest that perforin is a key mediator of axon injury and lend additional support to the hypothesis that $CD8^+$ T cells are primarily responsible for axon damage in MS.

Keywords

Axon injury; $CD8^+$ T cell; CNS inflammation; MHC class I; Multiple sclerosis; Perforin; Theiler's murine encephalomyelitis virus

INTRODUCTION

Evidence from patients with multiple sclerosis (MS) suggests that demyelination alone is insufficient to explain or predict the loss of neurologic function associated with the disease. Rather, the primary locus of permanent dysfunction is the axon without which information

*Correspondence: Charles Howe, PhD; Guggenheim 442-C; 200 First St. SW, Rochester, MN 55905. Voice: 507-538-4603; fax: 507-284-3383; howe.charles@mayo.edu.

cannot be transmitted through the neuraxis. It is unclear, however, whether MS is a primary oligodendrogliopathy, an axonopathy, or a combination of the two. Likewise, it is unclear whether axon injury is an obligatory consequence of demyelination or whether it is an active pathological process that is triggered by the immune system, the dysregulation of axonal electrophysiology, or both.

We previously observed that major histocompatibility complex (MHC) class I, $CD8^+$ T cells and perforin are implicated in the injury of demyelinated axons in the Theiler's murine encephalomyelitis virus (TMEV) model of MS (1–3). Likewise, $CD8^+$ T cells are implicated in MS (4,5), are associated with injured axons in demyelinated lesions (6) and they are able to transect axons in vitro (7). Moreover, MHC class I is expressed on neurons and axons in MS lesions (8). These findings suggest our working hypothesis that demyelination predisposes denuded axons to an MHC class I-restricted, $CD8^+$ T cell-mediated, perforin-dependent injury. To address this question, we elected to delete perforin expression genetically within the context of an MHC haplotype (H-2^q) that normally undergoes demyelination and loses motor function during chronic TMEV-induced disease. In contrast to previous studies, this tool eliminates the confounding effects of changes in viral persistence associated with manipulation of the $CD8^+$ T cell arm of the immune response in resistant mouse strains (3). Explicitly, a perforin-deficient H-2^q mouse allows us to determine whether demyelinated axons are preserved in the absence of one specific $CD8^+$ T cell effector mechanism and whether such preservation impacts neurologic function.

MATERIALS AND METHODS

Virus

The Daniel's strain of TMEV was used for all experiments (9). At 4 to 6 weeks of age, mice were inoculated intracerebrally with 2×10^5 PFU of TMEV in a total volume of 10 μL. The experimental design is outlined in Figure 1B.

Animals

C57BL/6-Pfp^{tm1sdz} mice (#002407, Jackson Laboratories, Bar Harbor, ME) have a targeted disruption of the perforin gene and are of the MHC class I H-2^b haplotype. $PFP^{-/-}$ H-2^q mice were generated by backcrossing the H-2^b perforin knockout mice to B10.D1-H2^q/SgJ mice (B10.Q #002024, Jackson Laboratories) (Fig. 1A). F_1 mice were mated to obtain F_2 breeding pairs, which were screened by PCR. Endogenous perforin was detected with forward primer IMR207 (5'-CCGGTCCTGAACTCCTGGCCAC-3') and the reverse primer IMR208 (5'-CCCCTGCACACATTACTGGAAG-3'). Mice with expression of wild type perforin generated a 300 base pair product by PCR. The targeted perforin allele was detected with forward primer IMR205 (5'-TTTTTGAGACCCTGTAGACCCA-3') and the reverse primer IMR206 (5'-GCATCGCCTTCTATCGCCTTCT-3'). In mice with the disrupted allele, PCR generated a 665 base pair product. Mice were further screened by flow cytometry using antibodies to H-2^b and H-2^q (BD Pharmingen, San Diego, CA). To establish the H-2^q line, we only bred mice that were negative for H-2^b. This line has been backcrossed more than 10 generations and all offspring are screened by both assays to confirm genotype. Gender was mixed for all experimental groups. Animal care and use were in accordance with IACUC and National Institutes of Health guidelines.

Isolation of Brain-Infiltrating and Spinal Cord-Infiltrating Leukocytes

Brain-infiltrating leukocytes (BILs) were isolated from mice at 7 days post-infection (dpi) by Percoll gradient, as described previously (10). In brief, whole brains were homogenized in 5 ml of RPMI on ice using a glass dounce homogenizer and brought to 20 ml final volume in RPMI. Homogenate was mixed with 10 ml Percoll (30%) (Pharmacia, Uppsala, Sweden) and

centrifuged at 27,000 × *g* for 30 minutes at 4°C. The myelin layer which floats in the 30% Percoll was removed and discarded. The leukocyte-enriched layer found at the bottom, just above the erythrocyte pellet, was removed and washed twice in RPMI; it was then resuspended in fluorescent activated cell sorter (FACS) buffer (PBS, 1% BSA, 0.2% sodium azide) and blocked for 20 minutes in FACS buffer containing 10% FBS and 50% supernatant from the 2.4G2 Fc blocking hybridoma.

Spinal cords were harvested from mice at various dpi; they were then homogenized and passed through a 70-μm-pore mesh strainer into RPMI to obtain a single cell suspension. The suspension was centrifuged at 800 × *g* for 5 minutes. The resulting pellet was resuspended in RPMI and fractionated using a step gradient consisting of 35% Percoll diluted in PBS, layered over 70% Percoll diluted in PBS, and centrifuged at 600 × *g* for 20 minutes. After centrifugation, leukocytes were removed from the interface between the 70% and 35% layers of Percoll. The cell suspension was diluted with RPMI and centrifuged at 1,200 × *g* for 5 minutes. The leukocyte-enriched cell pellet was resuspended in FACS buffer (PBS, 1% BSA, 0.2% sodium azide) and blocked for 20 minutes in FACS buffer containing 10% FBS and 50% supernatant from the 2.4G2 Fc blocking hybridoma. Flow cytometry was performed as previously described (10).

Analysis of Perforin and Granzyme B RNA

Total RNA from the BILs was isolated using a QIAshredder column and the RNeasy Mini Kit (Qiagen Inc., Valencia, CA). Whole brain was homogenized in RNA STAT-60 (1 ml per 100 mg tissue) (Tel-Test, Friendswood, TX) and total RNA was isolated according to directions. Perforin and granzyme B were amplified by RT-PCR using gene-specific primers. Perforin: forward (5'-AACAGAACCCGAAGC-3') and reverse (5'-GGACTCACACTCCCG-3'). Granzyme B: forward (5'-GCAAGTCATCCCTATGGT-3') and reverse (5'-GGACTCACACTCCCG-3'). RT-PCR was performed using the LightCycler SYBR Green I RNA amplification kit (Roche Applied Science, Indianapolis, IN) in glass capillaries containing 10 pmol primers, 6 mM $MgCl_2$, and 0.5 μg total RNA from whole brain or 0.1 μg total RNA from BILs. Sequential reaction conditions were: reverse transcription at 55°C for 30 minutes, denaturation at 95°C for 30 seconds, 30 cycles of amplification consisting of denaturation at 95°C without plateau phase, annealing at 57°C (perforin) or 59°C (granzyme) for 10 seconds, and extension at 72°C for 10 seconds. When the fluorescence signal in the melting temperature analysis rose above the background signal (crossing point determined automatically by the "fit points" method and arithmetic baseline adjustment for quantification by LightCycler 3.5 software supplied by Roche), samples were considered positive. Values are presented as change in crossing point values relative to uninfected samples (whole brain) or relative to the non-specific crossing point generated forcontrol samples lacking template RNA (BILs).

Analysis of Viral Load

The VP2 fragment of TMEV was amplified by reverse transcription (RT)-PCR with gene-specific primers from total RNA. The primer pair sequences for VP2 were: forward (5'-TGGTCGACTCTGTGGTTACG-3') and reverse (5'-GCCGGTCTTGCAAAGATAGT-3'). Glyceraldehyde-3-phosphate dehydrogenase (GAPDH) was used as a control for intersample variability. GAPDH primers were: forward (5'-ACCACCATGGAGAAGGC-3') and reverse (5'-GGCATGGACTGTGGTCATGA-3'). The sizes of the PCR products amplified with the primers were 238 bp for VP2 and 236 bp for GAPDH. Gene copy standards were analyzed with each set of samples. Standards were generated by serial 10-fold dilutions of plasmid and were amplified in parallel with the experimental samples by real-time quantitative RT-PCR with a LightCycler (Roche). Standards were plotted using a 3-parameter logistic curve fit algorithm in SigmaPlot and virus copy number in the experimental samples was calculated

using the equation for this curve. Negative controls (with input RNA omitted) were also used in each PCR run to confirm the specificity of the PCR products. PCR product curves were linear across serial 10-fold dilutions and the melting curve analysis indicated the synthesis of a single homogeneous product with the expected melting temperature. The reactions were carried out in 20 μL capillaries containing 7.0 mM $Mg2^{+}$, 10 pmol of forward and reverse primers, 4 μL of LightCycler RT-PCR SYBR green I mix (LightCycler RNA amplification kit SYBR green I; Roche), 2 μL of resolution solution, 0.4 μL of LightCycler RT-PCR enzyme mix, RNase-free H_2O, and 0.5 μg of total RNA. RT-PCR conditions for VP2 and GAPDH were: reverse transcription at 55°C for 10 minutes, denaturation at 95°C for 2 minutes, and 40 cycles of amplification. Amplification conditions were: denaturation to 95°C at 20°C/s without a plateau phase, annealing at 57°C for 7 seconds, and extension at 72°C for 15 seconds. The accumulation of product was monitored by SYBR green fluorescence at the completion of each cycle. There was a direct relationship between the cycle number at which the accumulation of PCR products became exponential and the log concentration of RNA molecules initially present in the RT-PCR. The reaction conditions for melting curve analysis were: denaturation to 95°C at 20°C/s without a plateau phase, annealing at 60°C for 5 seconds and denaturation to 95°C at 0.1°C/s, with continuous monitoring of SYBR green fluorescence. The amount of viral RNA was expressed as $\log_{10}$ virus copy number per 0.5 μg total RNA.

Immunostaining of Frozen Tissue

The whole brains were removed at 7 dpi, snap-frozen, and sectioned at 10 μm in a cryostat. Ethanol-fixed sections were blocked with 1% fetal calf serum and then incubated with primary antibodies against perforin (goat anti-perforin, C20; Santa Cruz Biotechnology, Santa Cruz, CA) and CD8 (rat anti-CD8b.2, Ly3.2; BD Pharmingen, San Diego, CA).

Immunostaining of Paraffin-Embedded Tissue

Mice were perfused via intracardiac puncture with 50 ml of 4% paraformaldehyde. Immunocytochemistry was performed on paraffin-embedded sections as previously described (2). Virus antigen staining was carried out using polyclonal antisera to TMEV that reacts strongly with the capsid proteins of the virus. Following incubation with a secondary biotinylated antibody (Vector Laboratories, Burlingame, CA), immunoreactivity was detected using the avidin-biotin immunoperoxidase technique (Vector Laboratories). The reaction was developed using Hanker-Yates reagent with hydrogen peroxide as the substrate (Polysciences, Warrington, PA). Slides were lightly counterstained with Mayer's hematoxylin.

Histopathologic Analysis of Brain and Spinal Cord Tissue

Mice were perfused via intracardiac puncture with 50 ml of Trump's fixative. Intact spinal column and skull were removed and post-fixed for 24 to 48 hours in Trump's fixative. Spinal cord and brain were removed and processed for plastic embedding (spinal cord) or paraffin embedding (brain). One-mm-thick coronal blocks of spinal cord were osmicated and embedded in glycol methacrylate; they were then sectioned at 2 μm and stained with a modified perichrome/cresyl violet stain (11). Spinal cord pathology was assessed on 12 to 15 sections of spinal cord per mouse, as previously described (12). Briefly, each quadrant from every coronal section from each mouse was graded for the presence or absence of gray matter disease, meningeal inflammation, and demyelination. The score was expressed as the percentage of spinal cord quadrants examined with the pathologic abnormality. A maximum score of 100 indicated that there was a particular pathologic abnormality in every quadrant of all spinal cord sections of a given mouse. All grading was performed without knowledge of the experimental group. Brain pathology was assessed as previously described (13). Pathology scores were assigned to cortex, corpus callosum, hippocampus, brainstem, striatum, and cerebellum using a 5-point scale: 0 = no pathology; 1 = no tissue destruction and minimal inflammation; 2 =

early tissue destruction (loss of parenchymal architecture) and moderate inflammation; 3 = definite tissue destruction (demyelination, frank parenchymal damage, cell death, neurophagia, neuronal vacuolization); 4 = necrosis (complete loss of all tissue elements and extensive debris). Meningeal inflammation was also assessed using a 5-point scale: 0 = no inflammation; 1 = 1 cell layer of inflammation; 2 = 2 cell layers of inflammation; 3 = 3 cell layers of inflammation; 4 = 3 or more cell layers of inflammation.

Axon Analysis

Axons were counted using our previously described protocol (2,3). Briefly, sections of araldite-embedded spinal cord were cut at 1 μm thickness and stained for exactly 20 minutes with the same batch of 4% para-phenylenediamine (PPD) to ensure an identical intensity of myelin labeling. Digitized images from the smallest thoracic spinal cord section (T6) were collected at 60× magnification from each animal according to a sampling scheme developed previously (2,3). Images were captured from regions containing no demyelination to ensure the measurement of only myelinated fibers. The thoracic spinal cord at T6 provides the highest ratio of spinal white matter to gray matter and also tends to be less frankly demyelinated as compared to cervical and lumbar spinal cord. Each field measured 17,675 μm^2; a total of 2.48 mm^2 from sham-infected controls, 1.98 mm^2 from perforin-competent mice, and 2.35 mm^2 from perforin-deficient mice were collected. Myelinated axon diameters were calculated following segmentation of the gray values corresponding to the axoplasm from each image. Batch algorithms were generated in Matlab (The Mathworks, Natick, MA) to calculate automatically the diameter of each axon in the field from the segmented binary image after regions corresponding to the vasculature, cell bodies, longitudinal axons and demyelination were excluded on the basis of circularity thresholding. Diameters less than 0.5 μm were excluded from the analysis to eliminate small regions that did not correspond to axons. Axon area measurements were binned for analysis: small = 1 to 4 μm^2; medium = 4 to 10 μm^2; large = >10 μm^2. The number of axons in each bin was normalized to the area of spinal cord analyzed to yield axons per mm^2. These values were averaged across all animals per group.

Measurement of Demyelinated Lesion Load in the Spinal Cord

Total white matter and demyelinated lesions in PPD-stained sections were traced by hand using a camera lucida system, followed by digitization and calculation of areas using Image J software. Measurements were made on 10 spinal cord sections from each animal. Percent demyelination was calculated by dividing the lesion area by the total white matter area and multiplying by 100.

Functional Analysis

The Rotamex rotarod (Columbus Instruments, Columbus, OH) was used to assess motor function. This device consists of a motor-driven rotating rod suspended 28.5 cm above an electrified grid. Mice were trained under a constant speed protocol and tested in an accelerating rod protocol according to our established procedures (2). On the day of testing the time to fall was recorded for each mouse; data were expressed as the percent decrease from baseline performance.

Statistics

All data are presented as mean ± 95% confidence interval with $\alpha = 0.05$. All statistical analyses were performed in SigmaPlot using the SigmaStat plug-in. RT-PCR and viral antigen distribution data were analyzed by t-test. Rotarod performance was analyzed by one-way (intra-group) and two-way (between groups) ANOVA with Student-Newman-Keuls post hoc pairwise analysis when appropriate. Flow cytometry, spinal cord pathology, viral load, and axon count data were analyzed by two-way ANOVA with Student-Newman-Keuls post hoc

pairwise analysis when appropriate. Brain pathology was analyzed by three-way ANOVA and the number of demyelinated mice was analyzed by Fisher's exact test.

RESULTS

Characterization of H-2^q Mice Deficient in Perforin

To address the function of perforin in animals with a susceptible MHC haplotype, we crossed PFP$^{-/-}$ H-2^b mice to B10.Q (B10.D1-H2^q/SgJ) mice (Fig. 1A). An F_2 generation was produced and animals homozygous for PFP$^{-/-}$ and H-2^q were selected. Homozygous PFP$^{-/-}$ and H-2^q-positive mice were intercrossed more than 10 generations to generate a line of PFP$^{-/-}$ H-2^q mice. In order to fully characterize the phenotype of these mice, we measured the levels of perforin mRNA in perforin-deficient and perforin-competent mice. Since we were looking specifically at perforin as an effector molecule, we used granzyme B mRNA levels as a control for the specificity of the genetic deletion. Perforin mRNA was not detected in the brain of perforin-deficient mice 7 days after infection with TMEV (a time when many CD8$^+$ cytotoxic T lymphocytes (CTLs) are present in the brain), but was expressed at high levels in the brain of perforin-competent mice infected for 7 d ($t(4)=13.877$, $p < 0.001$) (Fig. 1C). In contrast, granzyme B mRNA was abundantly expressed in the CNS of both perforin-deficient and perforin-competent mice at 7 dpi ($t(4)=-1.874$, $p = 0.143$) (Fig. 1C). GAPDH levels were the same between groups ($t(4)=0.152$, $p = 0.886$) (Fig. 1C). Next, we isolated brain-infiltrating leukocytes (BILs) from perforin-deficient and perforin-competent mice at 7 dpi using our established Percoll gradient technique (2). As with measurements made in the whole brain, we found that BILs exhibited no perforin expression in perforin-deficient mice, but such expression was easily detected in BILs derived from perforin-competent animals ($t(6)=16.228$, $P<0.001$) (Fig. 1D, F). Similarly, granzyme B was expressed in BILs in both groups of mice although there was a small but significant increase in granzyme B detected in perforin-deficient BILs ($t(6)=-2.756$, $p = 0.033$) (Fig. 1D). GAPDH levels were not different between groups ($t(6)=-0.117$, $p = 0.910$).

We also asked whether CD8$^+$ T cells were present at normal levels in the spinal cord white matter of mice deficient in perforin expression. This experiment was critical in supporting the conclusion that a factor secreted by CD8$^+$ T cells, rather than the removal of CD8$^+$ T cells, wasresponsible for the altered phenotype of these mice following TMEV infection. We found that both perforin-competent (Fig. 2A–C) and perforin-deficient (Fig. 2E–G) mice exhibited similar distributions of CD8$^+$ T cells within inflammatory foci in the spinal cord white matter during chronic infection. Perforin protein expression was assessed in chronically infected mice using double-labeling immunofluorescence to look for co-expression of CD8 and perforin within spinal cord-localized cytotoxic CTLs. Examination of frozen sections derived from the spinal cord of perforin-competent mice at 180 dpi indicated the presence of CD8$^+$ CTLs that also expressed perforin (Fig. 2D). In contrast, perforin-deficient mice exhibited numerous CD8$^+$ cells but no perforin expression (Fig. 2H). We verified that the number of infiltrating CD8$^+$ T cells did not depend upon perforin expression using flow cytometric analysis of spinal cord-infiltrating leukocytes (SCILs) at 7, 45, and 180 dpi. Representative examples of CD8$^+$CD45^{hi} cells present in SCILs isolated at 180 dpi are shown for perforin-competent (Fig. 2I) and perforin-deficient (Fig. 2J) mice. As indicated in Table 1, there was no significant difference between perforin-competent mice and perforin-deficient mice in percentages of infiltrating CD8$^+$ cells in the SCILs at any time point analyzed. We conclude that the phenotypic alterations observed in the perforin-deficient H-2^q line of mice are not the result of defects in expression or distribution of CD8$^+$ T cells within the CNS following infection.

Perforin-Deficient and Perforin-Competent Mice Exhibit Similar Levels of Gray Matter Disease in the Brain And Spinal Cord and Similar Levels of Demyelination Infection

Following TMEV infection there was no difference in survival in perforin-deficient mice as compared to perforin-competent mice ($F(1,261)=0.122$, $p = 0.741$, two-way ANOVA) (Fig. 3). No deaths from acute disease were observed in any of the infected mice and the extent of brain abnormalities was not different between the groups at any time point ($F(23,539)=0.942$, $p = 0.332$ between perforin-competent and perforin-deficient mice, 3-way ANOVA). We also compared the extent of gray matter pathology, white matter inflammation, and demyelination in the spinal cord in both groups at 7, 21, 45, 90, and 180 dpi (Table 2). Two-way ANOVA for strain and dpi revealed no significant differences in any measure at any time point. Additional post hoc pairwise comparisons between strains at each time point confirmed the absence of any differences in the percent of spinal cord quadrants showing gray or white matter inflammation or demyelination or in the number of mice exhibiting demyelination (Table 2). We also measured the total demyelinated lesion load in the spinal cord at 90 and 180 dpi in both strains and found no differences. At 90 dpi, perforin-deficient mice exhibited demyelination that occupied 29.0 ± 9.2% of the spinal white matter; perforin-competent mice had 32.0 ± 8.4% demyelination ($t(20)=-0.465$, $p = 0.647$). At 180 dpi, perforin-deficient mice had 41.7 ± 8.8% demyelination and perforin-competent mice had 38.6 ± 9.8% demyelinated lesion load ($t(20)=0.468$, $p = 0.645$). Histological examination of the brain and spinal cord showed that there were no qualitative differences in the extent of gray matter (Fig. 4A, B) or white matter (Fig. 4C–F) pathology between the groups. Thus, deletion of perforin had no effect on either early neuronal disease or late demyelinating disease in H-2^q mice. We conclude that the severity and distribution of spinal cord pathology does not account for phenotypic differences between perforin-deficient mice and perforin-competent mice.

Viral Load in Perforin-Deficient Mice Is not Different Compared to Perforin-Competent Mice

Recent reports indicate that viral RNA persists following TMEV infection during chronic disease even though it is often difficult to detect infectious virus by plaque assay (14). We used a sensitive and quantitative RT-PCR assay that allowed us to measure the copy number of VP2-specific RNA in the brain and spinal cord of infected mice (Table 3). GAPDH expression was monitored as an internal control in all experiments. The copy number of GAPDH mRNA was $\log_{10}$ 7.20 ± 0.02 in the brain and $\log_{10}$ 7.09 ± 0.03 in the spinal cord irrespective of perforin expression. We evaluated the level of virus RNA expression in the brain and spinal cord independently. In the brain during acute infection, both groups of mice had high expression of viral RNA (approximately 7 $\log_{10}$ copies) irrespective of perforin expression. Though viral clearance from the brain was delayed in perforin-deficient mice, viral load was essentially at the detection threshold in both groups by 45 dpi (Table 3). Likewise, there was persistence of VP2 RNA in the spinal cord irrespective of perforin expression. No difference in viral RNA expression was observed in the spinal cord in perforin-competent versus perforin-deficient mice at any time point ($F(1,34)=0.0225$, $p = 0.882$, two-way ANOVA) (Table 3). Overall, the level of viral RNA persistence in the spinal cord in both groups was approximately 5 to 6 $\log_{10}$ copies, consistent with the observation that prominent demyelination was observed in these mice irrespective of perforin expression.

We also examined the extent and distribution of TMEV antigen in the spinal cord of mice. The data are expressed as the percentage of spinal cord quadrants showing virus antigen-positive cells in either the gray matter or white matter of the spinal cord. In perforin-competent mice the virus was expressed primarily in the gray matter at 7 dpi (14.8 ± 4.7%), but then mostly in the white matter at 45 dpi (21.5 ± 5.7%) and at 180 dpi (12.4 ± 5.2%). A similar pattern was observed in perforin-deficient mice, with virus predominant in the gray matter at 7 dpi (5.8 ± 4.9%; P=0.2 vs. $PFP^{+/+}$), moving to the white matter by 45 dpi (14.4 ± 8.2%; $p = 0.5$ vs., $PFP^{+/+}$), and persistent in the white matter at 180 dpi (13.5 ± 7.5%; $p = 0.9$ vs. $PFP^{+/+}$).

Therefore, perforin deletion had no appreciable effect on the extent and distribution of TMEV antigen in the spinal cord throughout the course of disease. This indicates that viral persistence in the spinal cord is not substantially altered by perforin deletion and that viral load cannot account for phenotypic differences between the groups.

Neurologic Function Is Preserved in Demyelinated, TMEV-Infected Perforin-Deficient Mice

We used the rotarod to assess neurologic function in perforin-deficient and -competent mice, as described (2,3). Both groups used for this analysis exhibited demyelination in approximately 40% of spinal cord quadrants at 180 dpi (Table 2). The performance at 45 dpi did not differ between the groups (Fig. 5). In perforin-competent mice there was, however, a significant progressive decline in at 90 and 180 dpi ($F(2,63)=122.155$, $p < 0.001$; one-way ANOVA) whereas perforin-deficient mice exhibited preservation of function from 45 to 180 dpi. The differences in function between perforin-competent and -deficient mice at both 90 and 180 dpi were significant ($F(1,132)=210.186$, $p < 0.001$; two-way ANOVA). By 180 dpi, rotarod performance in mice lacking perforin was 3-fold higher than performance in perforin-competent mice ($PFP^{-/-}$ = 83.3 ± 3.1% of baseline; $PFP^{+/+}$ = 24.7 ± 6.8 % of baseline; $q(1,6)=19.529$, $p < 0.001$; SNK pairwise comparison) (Fig. 5). Therefore, the absence of perforin confers significant preservation of neurologic function despite the presence of robust spinal cord demyelination.

Spinal Axons Are Preserved in Perforin-Deficient Mice

Based on the observation that perforin-deficient mice exhibit preservation of neurologic function, we hypothesized that this preservation in perforin-deficient mice would correlate with a difference in the number of axons. Therefore, we counted numbers of small (1–4 μm^2 area), medium (4–10 μm^2 area), and large (>10 μm^2 area) caliber axons (3) in the mid-thoracic spinal cord of mice at 180 dpi. Small caliber axons were reduced in both perforin-competent and perforin-deficient mice at 180 dpi as compared to sham-infected wild type mice (Fig. 6A). Perforin-competent mice exhibited considerable loss of medium and large caliber axons (Fig. 6A, C, F, I, L, O), whereas perforin-deficient mice (Fig. 6A, D, G, J, M, P) did not differ significantly from sham-infected mice (Fig. 6A, B, E, H, K, N) ($F(2,164)=13.779$, $p < 0.001$ between groups; two-way ANOVA; SNK pairwise analysis isolated perforin-competent mice at $q(2,3)=14.866$, $p < 0.001$ vs. sham and $q(2,2)=12.102$, $p < 0.001$ vs. $PFP^{-/-}$). We conclude that perforin function leads to the loss of medium and large caliber spinal axons in the demyelinated spinal cord.

DISCUSSION

Our findings support the hypothesis that demyelination is necessary but insufficient for axon injury and loss of neurologic function in the TMEV model of MS. Our observations also indicate that the cytotoxic immune effector molecule perforin is a key mediator of injury to demyelinated axons. Genetic deletion of perforin led to the preservation of medium and large caliber spinal axons throughout the evolution of chronic demyelination. Axonal and functional preservation in perforin-deficient mice was not associated with a reduction or redistribution of demyelinated lesion burden, and viral load was not altered in chronically infected perforin-deficient animals. This suggests that the locus of preservation is the absence of perforin-mediated damage to demyelinated axons.

A number of previous studies have suggested that perforin, $CD8^+$ T cells, and MHC class I are important elements in the axon injury and loss of motor function that occurs in some strains of mice chronically infected with TMEV. These studies, however, were complicated by the use of mouse strains that are normally resistant to chronic TMEV infection, thereby confounding MHC haplotype-dependent effects on viral persistence and consequent

demyelination with mechanisms of axon injury. The absence of perforin in normally resistant H-2^b haplotype mice breaks resistance and leads to persistence of TMEV in the spinal cord and demyelination (3,15). Perforin-deficient H-2^b mice, however, do not exhibit the normal loss of motor function associated with demyelination in susceptible strains such as SJL and B. 10Q (3,15). Likewise, the absence of MHC class I expression in H-2^b (β_2-microglobulin-deficient) mice breaks resistance and leads to extensive spinal cord demyelination but preservation of motor function (1). In contrast, genetic deletion of MHC class II (Ab^0) in H-2^b mice breaks resistance and induces demyelination but also results in severe loss of motor function (1). Moreover, genetic deletion of either $CD8^+$ or $CD4^+$ T cells in H-2^b mice breaks resistance and triggers chronic demyelination, but whereas neurologic function is severely impaired and large spinal axons are lost in the $CD4^+$ T cell-deficient mice (3,16), function is preserved in $CD8^+$ T cell-deficient animals (16). These observations suggest a model in which $CD8^+$ T cells injure demyelinated axons in an MHC class I-dependent, perforin-dependent manner. Our current findings support this model and provide the additional benefit over these previous studies of preserving both the normal tropism of $CD8^+$ T cells into the demyelinated spinal cord and the normal ability of these T cells to form conjugates with targets and interact with targets via the Fas/FasL system and via cytokine release. The perforin-deficient H-2^q mouse model that we have generated circumvents the issue of changes in host resistance or susceptibility to virus and specifically tests the role of perforin within the context of an animal that normally develops demyelination during the chronic stage of infection.

Studies in the H-2^s haplotype SJL mouse and experiments using the BeAn strain of TMEV contradict some aspects of our observations. For example, CD8-deficient SJL mice exhibit more severe demyelination, enhanced inflammatory responses in the spinal cord and earlier onset of clinical disease; this suggests that these cells are regulatory or protective rather than injurious (17). Likewise, Kim et al reported that perforin-deficient H-2^b mice infected with the BeAn strain of TMEV develop not only robust demyelination but also clinical manifestations consistent with axon injury (18). These same investigators, however, observed that the absence of MHC class I and functional $CD8^+$ T cells resulted in chronic demyelination in the absence of neurologic deficits in H-2^b mice (19), a finding that was corroborated by Rossi et al (20). The discrepancies between these findings and the differences with our own observations may arise from alterations in the anti-viral response to BeAn antigens in perforin-deficient H-2^b mice, including greater $CD8^+$ T cell infiltration (18), enhanced antiviral antibody response (21), and enhanced cytokine responses in BeAn-infected mice (18).

Other models of axon injury also contradict some aspects of our findings. For example, Tsunoda and Fujinami favor an “inside-out” concept in which neuronal and axonal pathology precedes and triggers demyelination (22,23). An important aspect of this model is that axonal self-destruction is a protective mechanism for limiting the spread of neurotropic viruses (24). The preservation of axons and motor function that we observe in the absence of perforin, despite extensive demyelination, argues against the inside-out model, at least within the context of H-2^q mice. At the same time, we recognize that our study did not measure neuron and axon injury exhaustively, and it is therefore possible that some portion of the axon loss that we observe, (particularly small caliber axons), may occur as part of the host response to neuronal infection. We do not consider the inside-out and the perforin-mediated axonal injury models mutually exclusive; i.e. it is likely that a number of pathophysiological mechanisms underlie the loss of neurologic function in patients with MS. Indeed, our model does not exclude a role for anti-axonal autoimmunity (25,26), CD4-mediated axonal injury (27,28), antibody-mediated axon injury (29), or excitotoxic/metabolic mechanisms of axon damage (30–33); i.e. instead, we consider axonal injury the final common pathologic denominator reached by numerous mechanisms.

Several questions naturally arise from our present observations. Why are medium and large caliber axons spared in perforin-deficient hosts while small diameter axons are only fractionally protected? Which effector cell population is responsible for the perforin-mediated injury of axons? Is it possible that the absence of perforin in an effector cell population such as $CD8^+$ cytotoxic T cells alters another population of effectors that does not depend upon perforin, such as $CD4^+$ T cells? Assuming that the perforin effect is directly involved in axon injury, what is the mechanism by which the effectors recognize and attack the demyelinated axons? Is the cytotoxic event MHC class I-dependent, and, if so, are viral antigens or neural antigens relevant to the T cell receptor recognition? How would perforin directly injure axons? These questions are under ongoing consideration by our group but our current findings suggest that loss of myelin exposes denuded axons to an immune effector population that uses perforin to injure medium- and large-caliber spinal axons thereby eroding motor function. Therapeutic strategies aimed at protecting MS patients from long-term disability must contend with this pathogenetic process.

Acknowledgments

This work was supported by grants RG3636 (CLH), RG3172 (MR), and CA1011A8 (MR) from the National Multiple Sclerosis Society, by funding from Donald and Frances Herdrich (CLH), by an Early Career Development Award from the Mayo Clinic (CLH), and by grants P01 NS38468, R01 NS32129 (MR), and R01 NS24180 (MR) from the National Institutes of Health.

REFERENCES

1. Rivera-Quinones C, McGavern D, Schmelzer JD, et al. Absence of neurological deficits following extensive demyelination in a class I-deficient murine model of multiple sclerosis. Nat Med 1998;4:187–193. [PubMed: 9461192]
2. Howe CL, Ure D, Adelson JD, et al. CD8+ T cells directed against a viral peptide contribute to loss of motor function by disrupting axonal transport in a viral model of fulminant demyelination. J Neuroimmunol 2007;188:13–21. [PubMed: 17493690]
3. Howe CL, Adelson JD, Rodriguez M. Absence of perforin expression confers axonal protection despite demyelination. Neurobiol Dis 2007;25:354–359. [PubMed: 17112732]
4. Babbe H, Roers A, Waisman A, et al. Clonal expansions of CD8(+) T cells dominate the T cell infiltrate in active multiple sclerosis lesions as shown by micromanipulation and single cell polymerase chain reaction. J Exp Med 2000;192:393–404. [PubMed: 10934227]
5. Weiss HA, Millward JM, Owens T. CD8+ T cells in inflammatory demyelinating disease. J Neuroimmunol 2007;191:79–85. [PubMed: 17920696]
6. Bitsch A, Schuchardt J, Bunkowski S, et al. Acute axonal injury in multiple sclerosis. Correlation with demyelination and inflammation. Brain 2000;123(Pt 6):1174–1183. [PubMed: 10825356]
7. Medana I, Martinic MA, Wekerle H, et al. Transection of major histocompatibility complex class I-induced neurites by cytotoxic T lymphocytes. Am J Pathol 2001;159:809–815. [PubMed: 11549572]
8. Hoftberger R, Aboul-Enein F, Brück W, et al. Expression of major histocompatibility complex class I molecules on the different cell types in multiple sclerosis lesions. Brain Pathol 2004;14:43–50. [PubMed: 14997936]
9. Lipton HL. Theiler's virus infection in mice: An unusual biphasic disease process leading to demyelination. Infect Immun 1975;11:1147–1155. [PubMed: 164412]
10. Deb C, Howe CL. NKG2D contributes to efficient clearance of picornavirus from the acutely infected murine brain. J Neurovirol 2008;14:261–266. [PubMed: 18569460]
11. Pierce ML, Rodriguez M. Erichrome stain for myelin on osmicated tissue embedded in glycol methacrylate plastic. J Histotechnol 1989;12:35–56.
12. Rodriguez M. Immunoglobulins stimulate central nervous system remyelination: Electron microscopic and morphometric analysis of proliferating cells. Lab Invest 1991;64:358–370. [PubMed: 2002654]

13. Drescher KM, Murray PD, David CS, et al. CNS cell populations are protected from virus-induced pathology by distinct arms of the immune system. Brain Pathol 1999;9:21–31. [PubMed: 9989447]
14. Trottier M, Kallio P, Wang W, et al. High numbers of viral RNA copies in the central nervous system of mice during persistent infection with Theiler's virus. J Virol 2001;75:7420–7428. [PubMed: 11462014]
15. Murray PD, McGavern DB, Lin X, et al. Perforin-dependent neurologic injury in a viral model of multiple sclerosis. J Neurosci 1998;18:7306–7314. [PubMed: 9736651]
16. Murray PD, Pavelko KD, Leibowitz J, et al. CD4(+) and CD8(+) T cells make discrete contributions to demyelination and neurologic disease in a viral model of multiple sclerosis. J Virol 1998;72:7320–7329. [PubMed: 9696828]
17. Begolka WS, Haynes LM, Olson JK, et al. CD8-deficient SJL mice display enhanced susceptibility to Theiler's virus infection and increased demyelinating pathology. J Neurovirol 2001;7:409–420. [PubMed: 11582513]
18. Palma JP, Lee HG, Mohindru M, et al. Enhanced susceptibility to Theiler's virus-induced demyelinating disease in perforin-deficient mice. J Neuroimmunol 2001;116:125–135. [PubMed: 11438167]
19. Pullen LC, Miller SD, Dal Canto MC, et al. Class I-deficient resistant mice intracerebrally inoculated with Theiler's virus show an increased T cell response to viral antigens and susceptibility to demyelination. Eur J Immunol 1993;23:2287–2293. [PubMed: 8370406]
20. Fiette L, Aubert C, Brahic M, et al. Theiler's virus infection of beta 2-microglobulin-deficient mice. J Virol 1993;67:589–592. [PubMed: 8416386]
21. Zoecklein LJ, Pavelko KD, Gamez J, et al. Direct comparison of demyelinating disease induced by the Daniel's strain and BeAn strain of Theiler's murine encephalomyelitis virus. Brain Pathol 2003;13:291–308. [PubMed: 12946019]
22. Tsunoda I, Fujinami RS. Inside-Out versus Outside-In models for virus induced demyelination: Axonal damage triggering demyelination. Springer Sem Immunopathol 2002;24:105–125.
23. Tsunoda I, Kuang LQ, Libbey JE, et al. Axonal injury heralds virus-induced demyelination. Am J Pathol 2003;162:1259–1269. [PubMed: 12651618]
24. Tsunoda I. Axonal degeneration as a self-destructive defense mechanism against neurotropic virus infection. Future Virol 2008;3:579–593. [PubMed: 19079794]
25. Huizinga R, Heijmans N, Schubert P, et al. Immunization with neurofilament light protein induces spastic paresis and axonal degeneration in Biozzi ABH mice. J Neuropathol Exp Neurol 2007;66:295–304. [PubMed: 17413320]
26. Huizinga R, Linington C, Amor S. Resistance is futile: Antineuronal autoimmunity in multiple sclerosis. Trends Immunol 2008;29:54–60. [PubMed: 18182323]
27. Brunn A, Utermohlen O, Carstov M, et al. CD4 T cells mediate axonal damage and spinal cord motor neuron apoptosis in murine p0106-125-induced experimental autoimmune neuritis. Am J Pathol 2008;173:93–105. [PubMed: 18535178]
28. Shriver LP, Dittel BN. T-cell-mediated disruption of the neuronal microtubule network: correlation with early reversible axonal dysfunction in acute experimental autoimmune encephalomyelitis. Am J Pathol 2006;169:999–1011. [PubMed: 16936273]
29. Basso AS, Frenkel D, Quintana FJ, et al. Reversal of axonal loss and disability in a mouse model of progressive multiple sclerosis. J Clin Invest 2008;118:1532–1543. [PubMed: 18340379]
30. Black JA, Newcombe J, Trapp BD, et al. Sodium channel expression within chronic multiple sclerosis plaques. J Neuropathol Exp Neurol 2007;66:828–837. [PubMed: 17805013]
31. Dutta R, McDonough J, Yin X, et al. Mitochondrial dysfunction as a cause of axonal degeneration in multiple sclerosis patients. Ann Neurol 2006;59:478–489. [PubMed: 16392116]
32. Waxman SG. Axonal conduction and injury in multiple sclerosis: the role of sodium channels. Nat Rev Neurosci 2006;7:932–941. [PubMed: 17115075]
33. Young EA, Fowler CD, Kidd GJ, et al. Imaging correlates of decreased axonal Na+/K+ ATPase in chronic multiple sclerosis lesions. Ann Neurol 2008;63:428–435. [PubMed: 18438950]

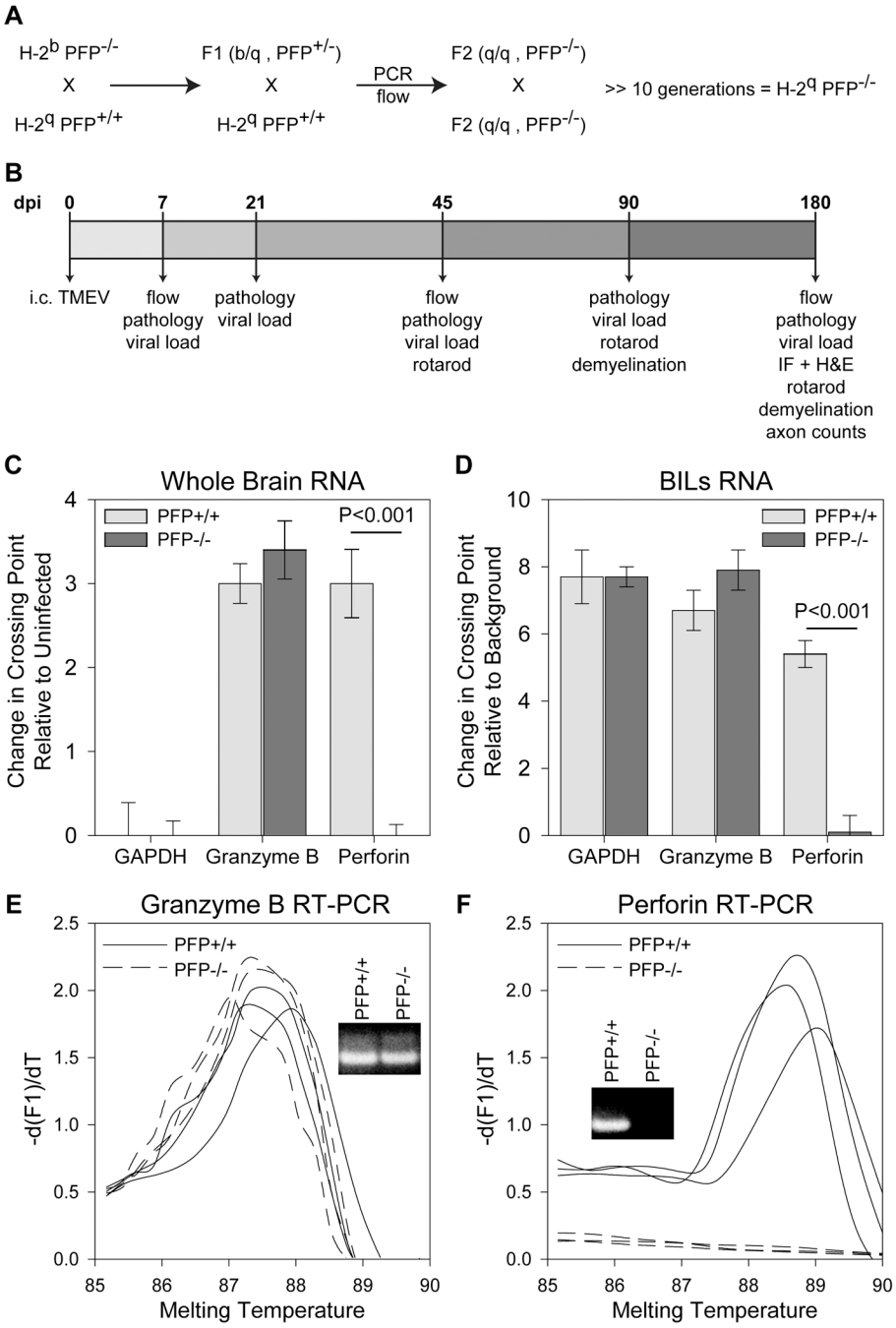

Figure 1.

Gene expression analysis in perforin-deficient mice. (**A**) Breeding strategy employed to generate the H-2^{q} perforin-deficient mice. (**B**) Experimental design utilized in this study. (**C–F**) Real-time RT-PCR analysis was performed on total RNA isolated from whole brain (**C**) or brain-infiltrating leukocytes (BILs) (**D–F**). (**C**) RNA was isolated from brain at 7 dpi and levels of GAPDH, granzyme B, and perforin were determined by RT-PCR. Glyceraldehyde 3-phosphate dehydrogenase (GAPDH) and granzyme B levels did not differ between the groups but perforin was not detected in perforin-deficient mice (n = 3 per group). Levels of gene expression are shown as mean change in crossing point relative to uninfected brain ± 95% confidence interval. (**D**) RNA was collected from BILs isolated at 7 dpi and levels of GAPDH,

granzyme B, and perforin were determined by RT-PCR. GAPDH did not differ between the groups. There was a small but significant ($p = 0.033$; $n = 3$ per group) increase in granzyme B in the perforin-deficient BILs. Perforin was not detected in the perforin-deficient BILs. Levels of gene expression are shown as mean change in crossing point relative to background ± 95% confidence interval (uninfected mice do not have sufficient BILs for analysis). (**E**) Representative granzyme B amplicon melting curves and PCR products (inset) are shown for 3 mice in each group. (**F**) Representative perforin amplicon melting curves and PCR products (inset) are shown for 3 mice in each group. A perforin product was not observed in the perforin-deficient BILs. Expression differences were analyzed by t-test. IF = immunofluorescence; H&E = hematoxylin and eosin.

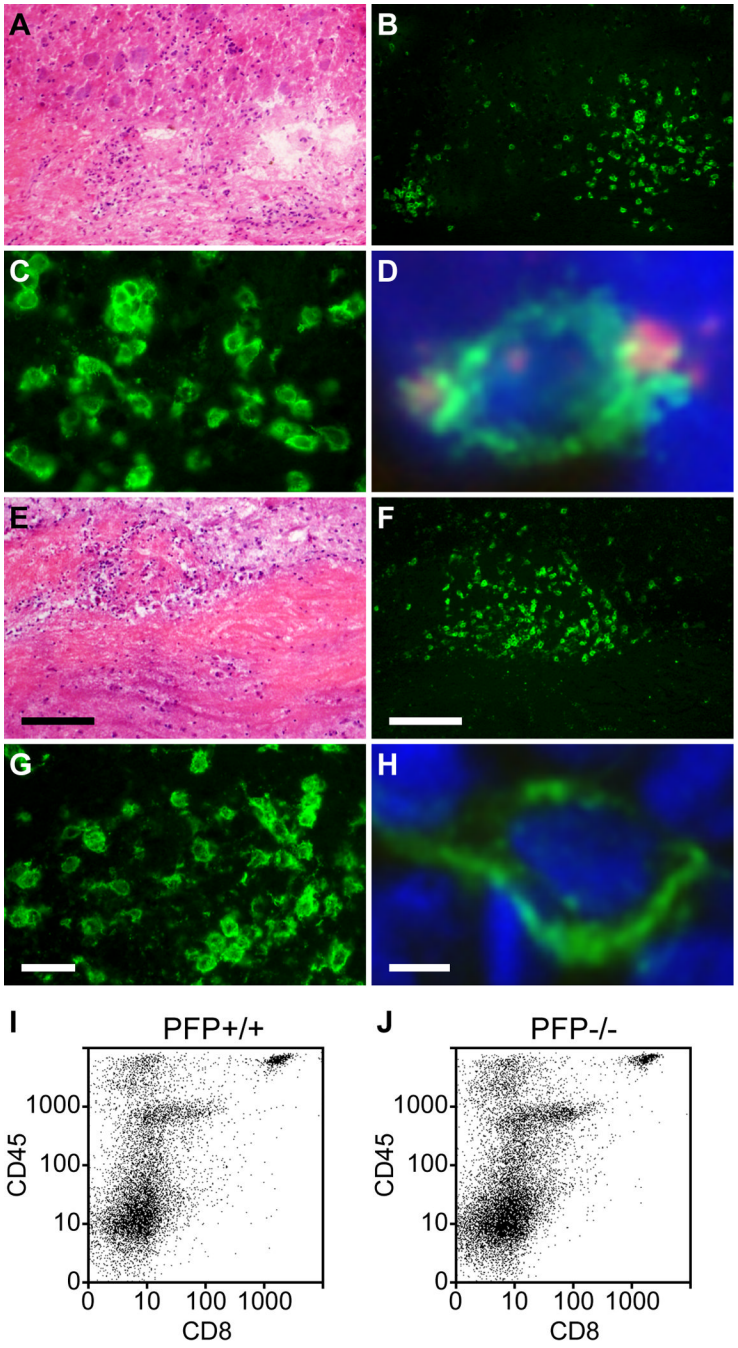

Figure 2.

$CD8^+$ cells infiltrate the spinal cord in chronically demyelinated mice irrespective of perforin expression. Spinal cord sections were prepared from perforin-competent (**A–D**) and perforin-deficient (**E–H**) mice at 180 dpi. (**A–H**) Representative inflammatory lesions in white matter are shown by hematoxylin and eosin stain (**A, E**). The lesions contain many cells that are immunopositive for CD8 in both perforin-competent (**B, C**) and perforin-deficient mice (**F, G**). Perforin co-staining (red) was observed in $CD8^+$ cells (green) within demyelinated lesions in perforin-competent mice (**D**) but not in perforin-deficient mice (**H**); blue indicates DAPI. (**I, J**) Flow cytometric analysis at 180 dpi confirmed that the number of $CD45^{hi}CD8^+$ cells present within isolated spinal cord infiltrating leukocytes did not differ between perforin-

competent (**I**) and perforin-deficient mice (**J**). Scale bar in E = 50 μm and also refers to A. Scale bar in F = 50 μm and refers to B. Scale bar in G = 10 μm and refers to C. Scale bar in H = 1 μm and refers to D. dpi = days post-infection

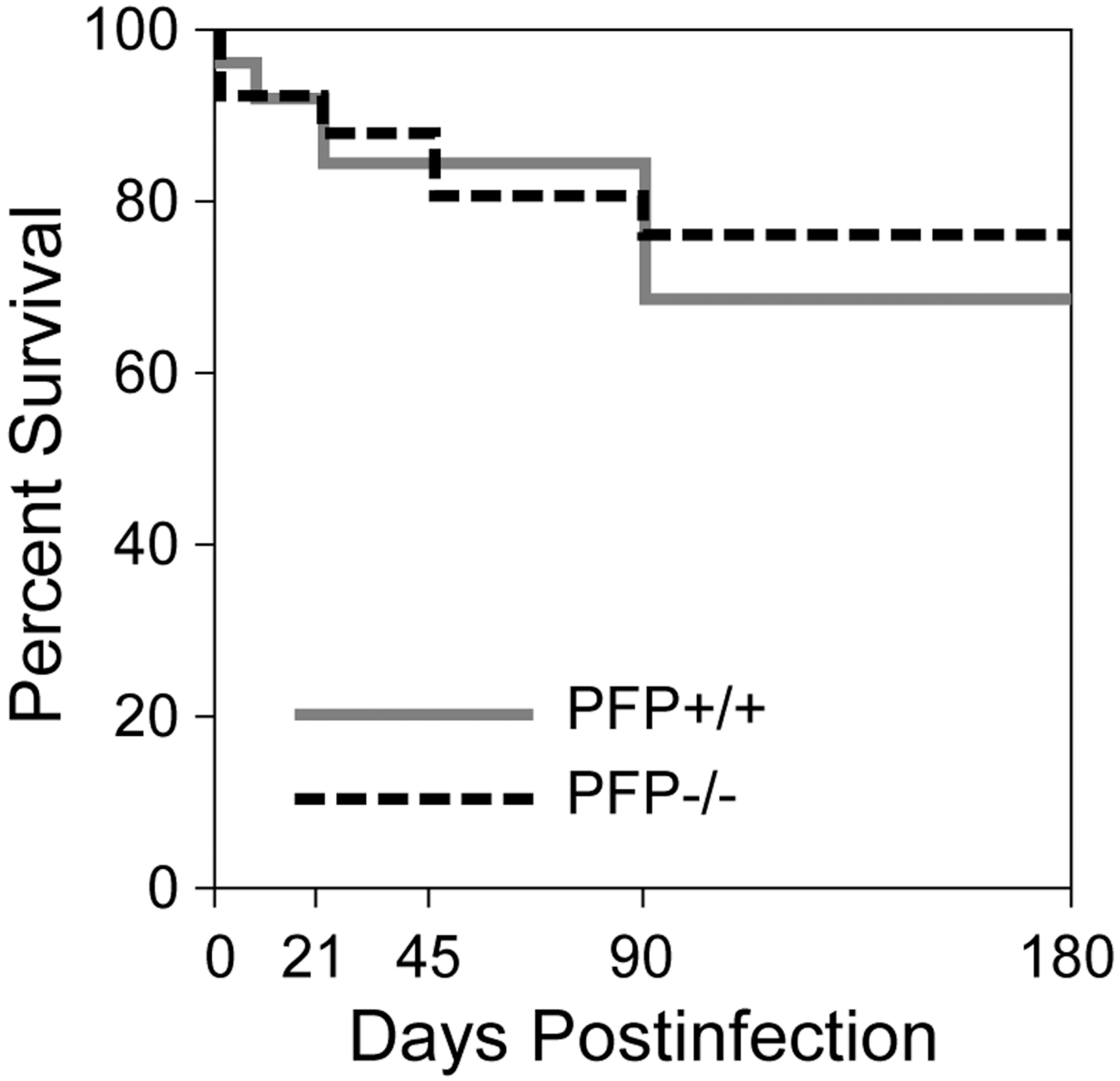

Figure 3.
Survival following Theiler's murine encephalomyelitis virus infection is not altered by the absence of perforin. Survival was assessed through 180 days post-infection (dpi) in perforin-competent (solid grey line) and perforin-deficient (dashed line) mice. Two-way ANOVA revealed no statistically significant difference between the groups at any time point ($p = 0.741$; $n = 15$ per group at 0 dpi).

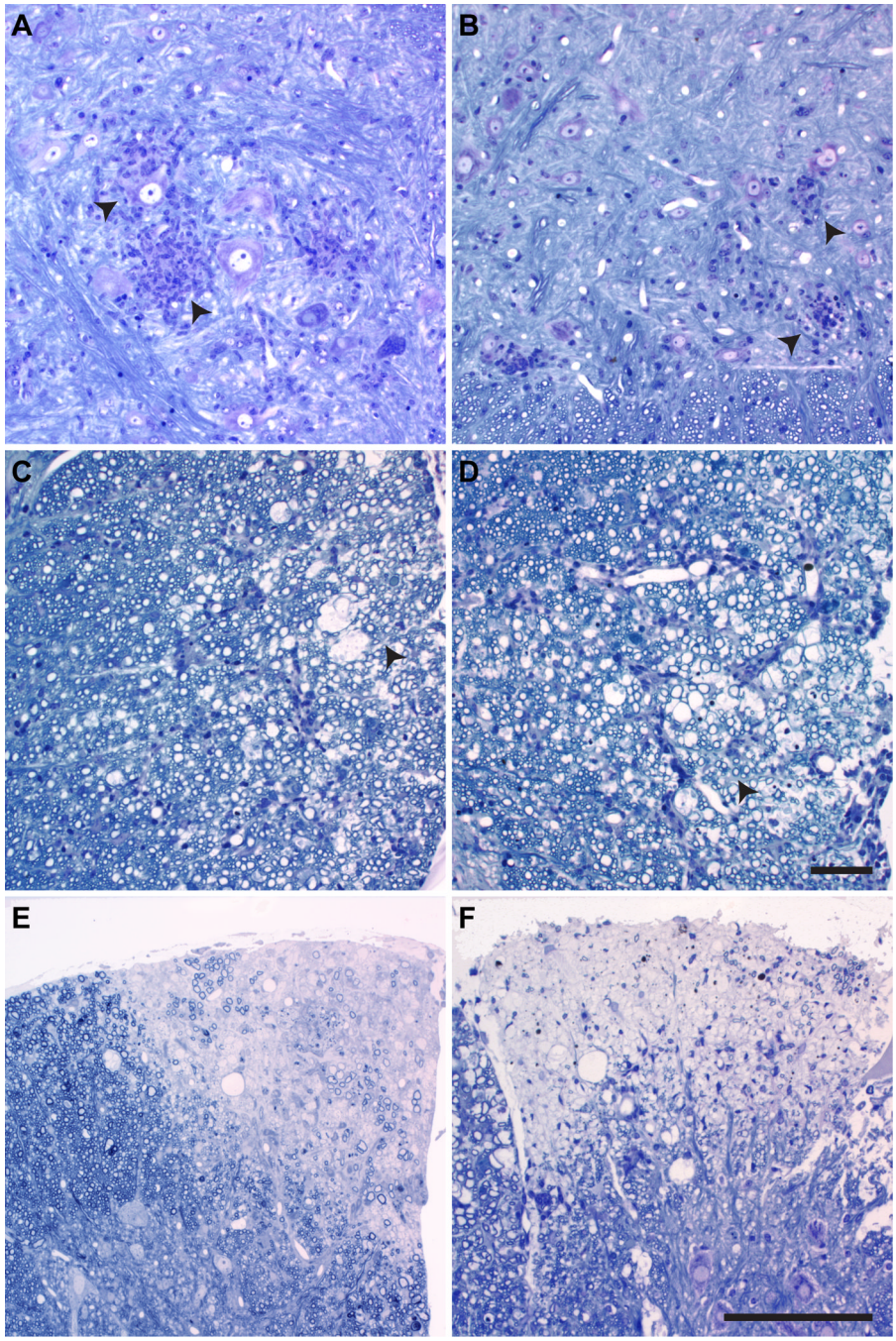

Figure 4.

Spinal cord histopathology. Pathologic features in the spinal cord gray matter (**A, B**) and white matter (**C–F**) in perforin-competent mice (**A, C, E**) and perforin-deficient mice (**B, D, F**) at 7 days post-infection (dpi) (**A, B**), 45 dpi (**C, D**) and 180 dpi (**E, F**) in plastic-embedded sections stained with erichrome and cresyl violet. Acute neuronal disease, as suggested by neuronal swelling and inclusions and the proximity of numerous inflammatory cells is seen in both perforin-competent (arrowheads in **A**) and perforin-deficient (arrowheads in **B**) mice. Early demyelination (45 dpi) was morphologically similar between perforin-competent (**C**) and perforin-deficient (**D**) mice; arrowheads mark the general region of myelin damage. By 180 dpi, the appearances of the lesions (pale areas) did not differ between perforin-competent (**E**)

and perforin-deficient (**F**) mice. Images were taken from mid-thoracic level and are representative of 10 mice in each group. Scale bar in D = 10 μm and refers to A–D. Scale bar in F = 50 μm and refers to E and F.

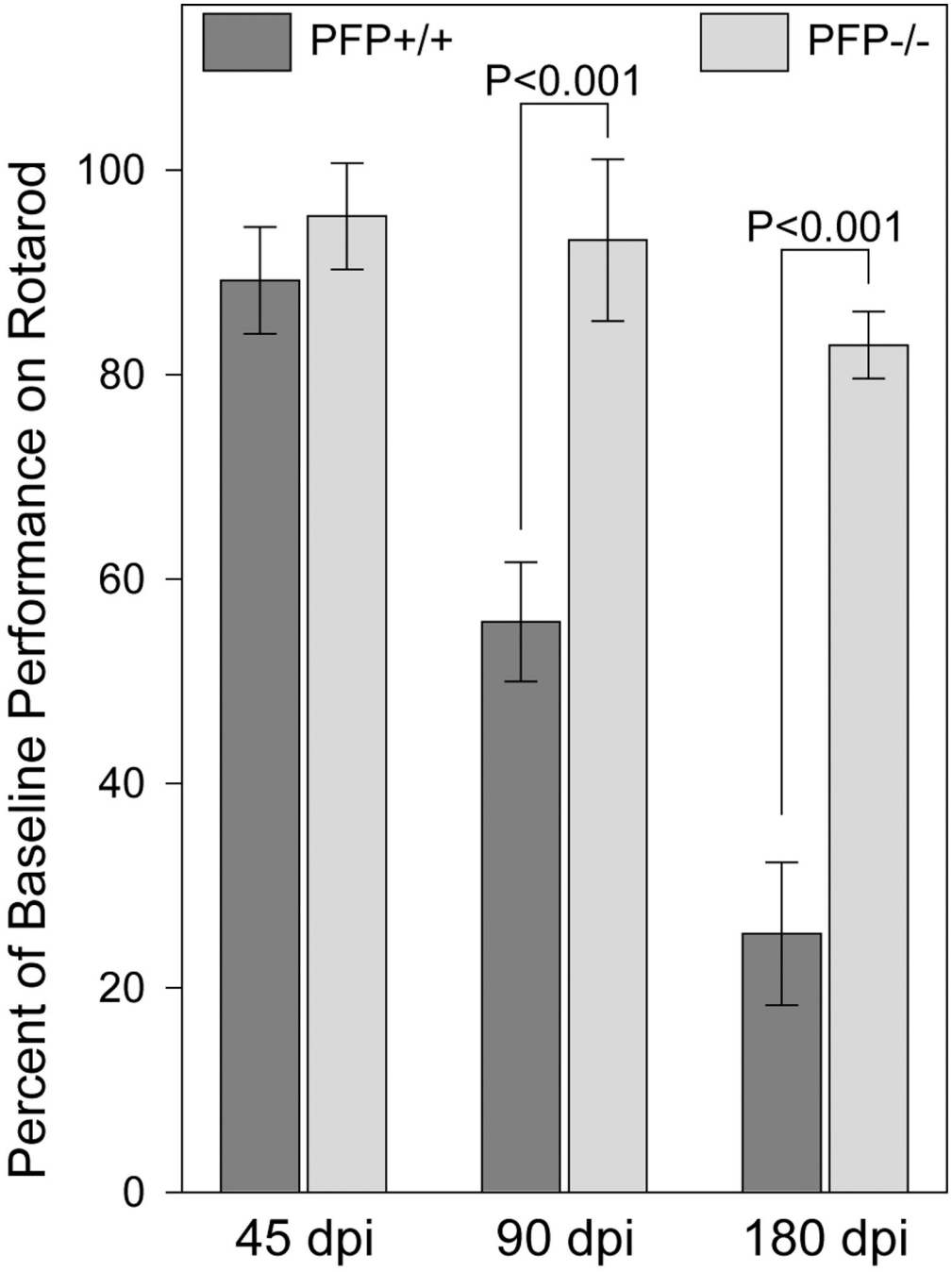

Figure 5.

Neurologic function is preserved in perforin-deficient mice following Theiler's murine encephalomyelitis virus infection and chronic demyelination. Rotarod performance was measured in perforin-competent (dark gray) and perforin-deficient (light gray) mice at 45, 90, and 180 days post-infection (dpi). Performance of 24 mice in each group that were followed longitudinally is shown as mean percent of baseline time-to-fall ± 95% confidence interval. Dead mice were retrospectively removed from the analysis; at 180 dpi, there were 19 perforin-competent and 22 perforin-deficient mice. Motor function was preserved in perforin-deficient mice throughout the course. P-values are derived from 2-way ANOVA.

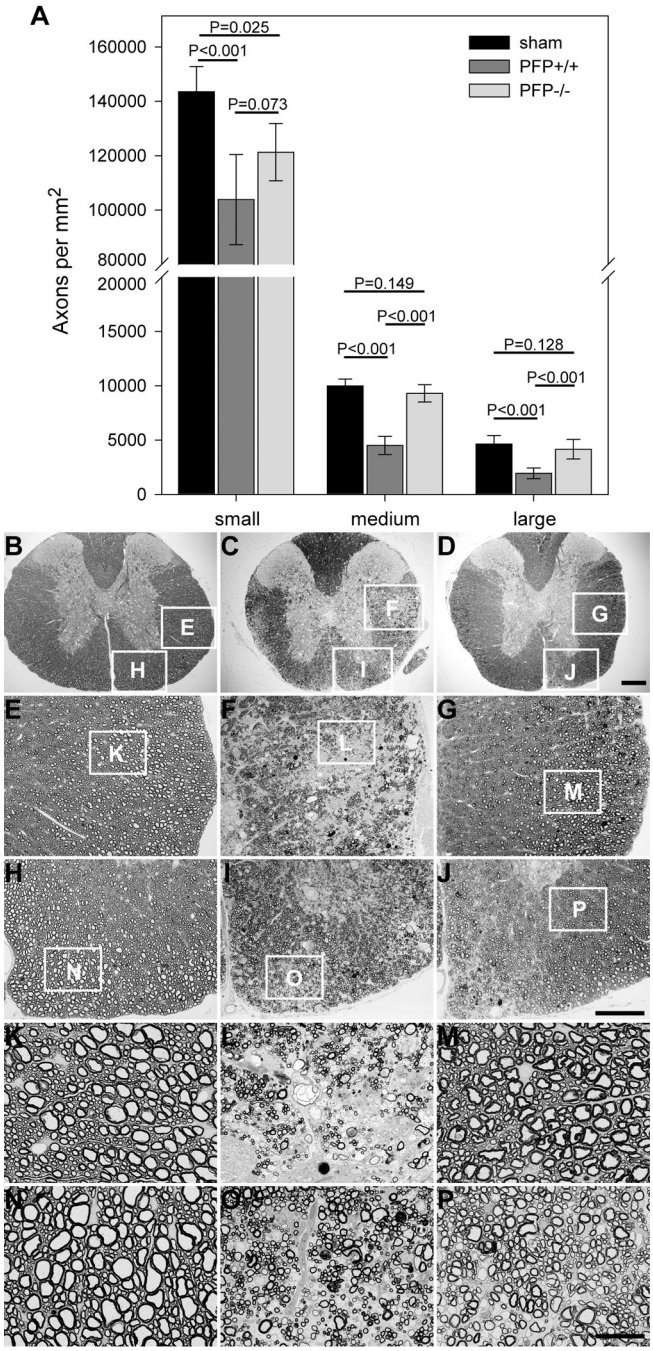

Figure 6.

Medium and large caliber spinal axons are preserved in perforin-deficient mice following Theiler's murine encephalomyelitis virus (TMEV) infection and chronic demyelination. The absolute numbers of myelinated axon profiles were determined at the mid-thoracic level in the spinal cord of sham-infected wild type mice (black bars) and TMEV-infected perforin-competent (dark gray bars) and perforin-deficient (light gray bars) mice at 180 days postin-fection(dpi) (**A**). Axon counts are shown as mean ± 95% confidence interval derived from 20 sham, 16 perforin-competent, and 19 perforin-deficient mice. Small = 1–4 μm^2 area; medium = 4–10 μm^2 area; large = >10 μm^2 area. Representative images of mid-thoracic spinal cord araldite sections are shown at several magnifications for sham-infected (**B, E, H, K, N**) and

TMEV-infected perforin-competent (**C, F, I, L, O**) and perforin-deficient (**D, G, J, M, P**) mice at 180 dpi. White boxes in **B–J** indicate the location of subsequent higher magnification panels. There is considerable loss of axons in both lateral (**F, L**) and ventral (**I, O**) white matter tracts in the perforin-competent animal. Preservation of medium and large axons is clear in the lateral (**G, M**) and ventral (**J, P**) cord in the perforin-deficient mouse. Scale bar in D = 200 μm and refers to B–D; scale bar in J = 100 μm and refers to E–J; scale bar in P = 25 μm and refers to K–P. P values derive from one-way ANOVA between strains for each axon size group.

Table 1

Flow Cytometric Analysis of CNS-Infiltrating Lymphocytes

Days Postinfection	Material Analyzed	Strain	Percent of $CD8^+$ Cells in $CD45^{hi}$ Population	Number of Samples	P-value ($^{+/+}$ vs $^{-/-}$)
7	BILs	$PFP^{+/+}$	16.6 ± 1.9	4	p = 0.686
		$PFP^{-/-}$	17.2 ± 2.2	4	
45	SCILs	$PFP^{+/+}$	33.3 ± 7.8	4	p = 0.732
		$PFP^{-/-}$	31.7 ± 3.7	4	
180	SCILs	$PFP^{+/+}$	27.0 ± 8.1	4	p = 0.560
		$PFP^{-/-}$	30.8 ± 8.8	4	

Brain-infiltrating lymphocytes (BILs) and spinal cord-infiltrating lymphocytes (SCILs) were collected and analyzed as described in Methods. Data are mean ± 95% confidence interval (CI) for percent of $CD45^{hi}$ cells that were $CD8^+$. Two-way ANOVA revealed no difference between strains (p = 0.402). P values represent between-strain pair-wise comparisons. There was no statistical difference between strains at any time point analyzed.

Table 2

Analysis of Spinal Cord Pathology

Mouse Strain	Day*	N#	Gray Matter Inflammation		White Matter Inflammation		Percent of Quadrants with Demyelination		Number of Mice with Demyelination	
$PFP^{+/+}$	7	11	6.6 ± 4.5		2.6 ± 3.1		0.2 ± 0.3		1/11	
$PFP^{-/-}$	7	10	9.7 ± 8.6	P=0.55@	4.6 ± 4.3	P=0.48	0.0 ± 0.0	P=0.391	0/10	P=1.00
$PFP^{+/+}$	21	11	2.2 ± 2.2		10.0 ± 7.4		1.0 ± 0.9		4/11	
$PFP^{-/-}$	21	18	0.6 ± 0.8	P=0.12	8.8 ± 6.3	P=0.82	2.0 ± 2.5	P=0.534	9/18	P=0.702
$PFP^{+/+}$	45	12	0.0 ± 0.0		7.7 ± 3.3		25.4 ± 6.1		12/12	
$PFP^{-/-}$	45	12	0.0 ± 0.0	P=1.00	11.1 ± 4.1	P=0.13	27.8 ± 8.6	P=0.663	12/12	P=1.00
$PFP^{+/+}$	90	13	0.0 ± 0.0		14.3 ± 10.2		30.8 ± 6.8		13/13	
$PFP^{-/-}$	90	20	0.0 ± 0.0	P=1.00	17.7 ± 8.2	P=0.61	32.3 ± 5.7	P=0.751	20/20	P=1.00
$PFP^{+/+}$	180	15	0.0 ± 0.0		11.6 ± 4.9		42.3 ± 5.9		15/15	
$PFP^{-/-}$	180	19	0.0 ± 0.0	P=1.00	13.4 ± 12.9	P=0.82	45.4 ± 5.3	P=0.448	19/19	P=1.00

*Days after infection

#Number of mice

@PFP−/− vs. PFP+/+

Spinal cords from infected $PFP^{-/-}$ or $PFP^{+/+}$ mice were processed for microscopy and examined as described in Methods. Morphological analysis was performed on 12 to 15 sections per mouse. Values are percent of spinal cord quadrants examined with the pathologic abnormality ± 95% CI and as number of mice per group exhibiting demyelination. Inflammation and demyelination quadrant data were analyzed by two-way ANOVA, followed by Mann-Whitney rank sum or t-test pair-wise comparison. No difference in strain was isolated at any time point for percent demyelination (p = 0.381). Data for number of demyelinated mice were analyzed by the Fisher exact test. There were no significant differences in any pathological parameter at any time point.

Table 3

Viral Load In Brain and Spinal Cord of Perforin-Competent and -Deficient Mice

Tissue	dpi*	Strain	VP2 copy #	Statistics^
Brain	7	$PFP^{+/+}$	6.6 ± 1.6	
		$PFP^{-/-}$	7.3 ± 1.1	p = 0.576
	21	$PFP^{+/+}$	2.1 ± 2.1	
		$PFP^{-/-}$	5.7 ± 0.6	p = 0.035
	45	$PFP^{+/+}$	0.6 ± 1.3	
		$PFP^{-/-}$	1.5 ± 3.0	p = 0.620
	90	$PFP^{+/+}$	0.8 ± 1.4	
		$PFP^{-/-}$	0.8 ± 1.6	p = 0.978
	180	$PFP^{+/+}$	0.6 ± 1.5	
		$PFP^{-/-}$	1.7 ± 1.8	p = 0.334
Spinal Cord	7	$PFP^{+/+}$	5.7 ± 0.2	
		$PFP^{-/-}$	5.4 ± 0.5	p = 0.382
	21	$PFP^{+/+}$	5.2 ± 0.9	
		$PFP^{-/-}$	5.9 ± 0.5	p = 0.281
	45	$PFP^{+/+}$	5.8 ± 0.2	
		$PFP^{-/-}$	5.1 ± 1.2	p = 0.301
	90	$PFP^{+/+}$	5.6 ± 0.8	
		$PFP^{-/-}$	4.8 ± 0.3	p = 0.131
	180	$PFP^{+/+}$	4.4 ± 1.3	
		$PFP^{-/-}$	5.4 ± 1.8	p = 0.444

* Days post-infection

^ post-ANOVA pair-wise analysis

Viral RNA expression was analyzed at the indicated days post-infection in the brain and spinal cord of $PFP^{+/+}$ and $PFP^{-/-}$ mice. Values are reported as mean $\log_{10}$ copy number ± 95% CI for 3 animals per group. The detection threshold for this assay is 0.61 ± 0.58 $\log_{10}$ copies, as measured in uninfected brain and spinal cord samples. The early difference in viral load observed in the brain (21 dpi) is compatible with delayed viral clearance associated with the lack of perforin effector function. Based on this difference two-way ANOVA identified a weak strain dependence on viral load in the brain ($p = 0.048$). By 45 dpi the virus was essentially cleared from the brain. In the spinal cord, there were no differences between the groups. Two-way ANOVA revealed no effect of strain on viral load in the spinal cord ($p = 0.882$). Levels of expression of control GAPDH RNA were not different between the groups at any time point.